Journal of Physics B: Atomic, Molecular and Optical Physics

PAPER • **OPEN ACCESS**

L-M*n* dielectronic recombination of cerium ions in a room-temperature EBIT

To cite this article: W Biela-Nowaczyk *et al* 2024 *J. Phys. B: At. Mol. Opt. Phys.* **57** 055201

OPEN ACCESS
IOP Publishing
Journal of Physics B: Atomic, Molecular and Optical Physics
J. Phys. B: At. Mol. Opt. Phys. **57** (2024) 055201 (9pp)
https://doi.org/10.1088/1361-6455/ad2b72

L-M*n* dielectronic recombination of cerium ions in a room-temperature EBIT

W Biela-Nowaczyk[1,2,*], F Grilo[3], P Amaro[3] and A Warczak[2]

[1] GSI Helmholtzzentrum für Schwerionenforschung, Darmstadt 64291, Germany
[2] Institute of Physics, Jagiellonian University, Cracow 31-007, Poland
[3] Laboratory of Instrumentation, Biomedical Engineering and Radiation Physics (LIBPhys-UNL), NOVA School of Science and Technology, NOVA University Lisbon, Caparica 2829-516, Portugal

E-mail: w.biela-nowaczyk@gsi.de and f.grilo@campus.fct.unl.pt

Received 28 September 2023, revised 16 January 2024
Accepted for publication 21 February 2024
Published 4 March 2024

Abstract

We explore the dielectronic recombination structures at the electron beam ion trap at Jagiellonian University in Cracow, emited by cerium that is produced by the high-current cathode made of iridium and cerium. Small amounts of these elements evaporate from the cathode and form low-intensity admixtures within the electron-ion plasma in the EBIT. Their presence and specific ionic population can be observed by examining the spectral characteristics resulting from the DR process. Results have been compared with flexible atomic code calculations, working in unresolved transition array mode, providing identification of the charge states. Here we show that this mode provides quick calculations of very complex data with enough reliability for experimental comparison. These observations highlight which DR features and corresponding charge states that should be present in spectra obtained in EBITs with similar cathode specifications.

Keywords: dielectronic recombination, electron beam ion trap, EBIT, flexible atomic code

1. Introduction

Cerium is an element of interest for several scientific areas, requiring precise spectroscopic data. On the one hand, cerium may be employed in plasma-facing components [1], hence, can potentially evaporate to plasmas and be spectroscopically observed in plasma environments, such as in fusion reactors. On the other hand, cerium and other lanthanide elements have astrophysical significance [2–4]. Recent discussions suggest the presence of this element in kilonovae [5, 6], although with low charge state. Moreover, this element is often used in cathodes for ion sources, such as electron cyclotron resonance ion sources, or electron beam ion trap (EBIT). Therefore, spectroscopy data for highly charged ions (HCI) of this element is needed for accurate interpretation of spectra emitted by ion sources [7]. For example, the observation of emissions from HCI of cerium and iridium impurities arising from a cathode with the same material has been reported [8], in a main magnetic focus ion source. Emission of HCI of cerium were also reported in an EBIT from contamination arising from a similar cathode [9].

Apart from this element, the EBIT device is a common tool for studying the emission and respective charge state distributions for a variety of elements. For example, there have been observations of HCI of tungsten ions [10–12] for fusion science applications, as well as gold [13] and sulfur [14] for charge state distribution quantification and applications in astrophysical plasmas.

With the use of an EBIT at Jagiellonian University, we investigated the spectroscopic signatures of cerium in the plasma present at the trap. The cathode used for electron beam production is made of iridium and cerium [9] and both of these

* Author to whom any correspondence should be addressed.

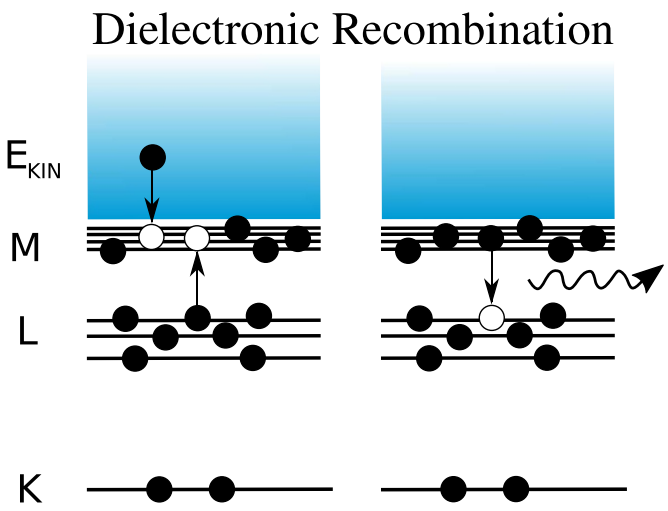

Figure 1. The schematic diagram of the L-MM DR process.

elements are present in plasma, with an amount dependent on the cathode current and EBIT vacuum conditions. Two distinct spectra were recorded at different residual pressures to observe emissions with different charge state populations. Here, we investigate the dielectronic recombination (DR) produced by this element for the particular cases of L-M*n* processes and report charge state populations.

The DR process occurs when ions and electrons collide, resulting in resonant capture, followed by photon emission. It is a fundamental atomic process and studying it in heavy ions like cerium can provide valuable insight into the complex dynamics of electron-ion interaction, electron correlation effects, and electron recombination processes in a multi-electron system. DR is a two step resonant process, its schematic diagram is presented in figure 1. The classical Auger nomenclature is adopted within this article, where L-MM means the excitation of an electron from the L shell to the M shell while simultaneously capturing a free electron into the M shell. The photon energies resulting from the radiative de-excitation of the intermediate state depend on the resonant energies (shells involved) as well as the charge state of the ion in which the process occurs. The DR process can be described schematically as follows:

$$A^{q+} + e^- \rightarrow A^{(q-1)+*} \rightarrow A^{(q-1)+} + \hbar\omega. \qquad (1)$$

The initial step of DR is often referred to as dielectronic capture (DC), which is the reverse process of Auger decay. During this step, a free electron is captured into a bound state of the ion, causing the simultaneous excitation of another bound electron. This leads to the formation of an excited state of the ion, known as the intermediate state. In the subsequent step of DR, the excited ion undergoes radiative stabilization. The observation of DR resonances has been done frequently in EBIT devices with HCI. To name a few examples, there are reports of observations of K-LL and L-MM in gold [15, 16], K-LL of several charge states of xenon [17], K-LL in H-like krypton [18], K-L*n* of several charge states of silicon [19] and L-M*n* of Ne-like iron [20–22]. In this work, we observed the L-M*n* resonant structure of Ce^{33+} to Ce^{41+} with $n = $ M, N, O.

Flexible atomic code (FAC) was used to identify the charge states and the respective resonances. Here, we show that calculations in unresolved transition array mode (UTA), which significantly reduce the complexity and time of DR calculations, can still provide reliable charge identification of DR complex spectra.

2. Methods

2.1. Experimental setup

This experiment was conducted at Jagiellonian University (UJ) using a compact, room-temperature EBIT with permanent magnets. The UJ-EBIT is an S model of ion irradiation facility provided by the commercial DREEBIT company. The schematic diagram of the trap can be seen in figure 2. More information about the used apparatus can be found in [23, 24].

The x-ray spectrum was collected with the use of a silicon-drift detector (SDD) from Bruker (XFlash Bruker 5030). The SDD offered an energy resolution of 127 eV FWHM (full-width at half-maximum) at the Mn K_α line and had an active area of 30 mm^2. The detector was previously calibrated with radioactive sources and tested in several experiments. It was positioned perpendicular to the beam axis at the center of the trap. Both the trap and the detector were equipped with combined Be windows measuring 25 μm. The highest efficiency of photon detection ($\geqslant 90\%$) is for the energy range of 3–12 keV [25]. Additionally, our acquisition system, which relied on the TERX detection system [26], enabled the electron energy scanning during the data collection.

The cathode used to produce the electron beam in the EBIT is composed of iridium and cerium. These elements are observed in trace amounts inside the trap. The EBIT apparatus operates under conditions of ultra-high vacuum, with a background level of 10^{-10} mbar. The buffer gas (here neon) can be introduced into the apparatus using a micrometer screw, which allows a precise control of the residual pressure in the trap during experiments. The residual pressure variation influences significantly the plasma dynamics in the EBIT and affects the concentration of highly charged states in the ion mixture. The presence of a buffer gas leads to an increase in the intensity of the charge exchange (CX) process. This is one of the main processes responsible for reducing the ionization level in the EBIT plasma. Consequently, in the case of higher residual pressure, the charge distribution tends to be less ionized.

The cathode works at high operating temperatures and, as a result, the constituent elements evaporate and enter the rest gases of the trap. The interaction of this heavy elements with the electron beam can lead to their ionization and fluorescence. Based on the preliminary experiments, the preferable working conditions of the used EBIT for the presented experiment were chosen to be in the range of 2300–4500 eV. In this energy range it is possible to partly ionize the M-shell of cerium ions. Moreover, the L-shell x-ray series, which is

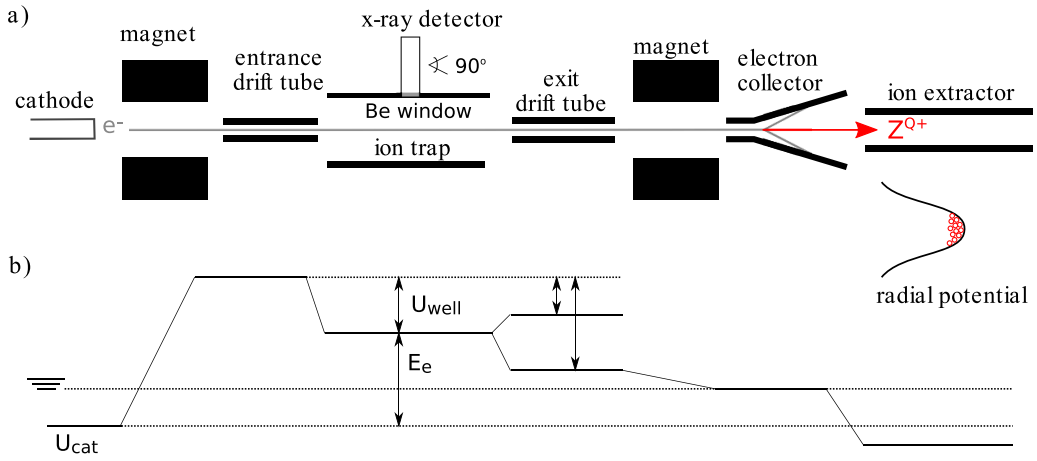

Figure 2. (a) Schematic of the Model S EBIT (DREEBIT). (b) Representation of all voltages at each electron beam stage. Reproduced from [23]. CC BY 4.0.

a signature of the L-Mn DR process for this element is located in the photon energy range of 4.5–8 keV, which is preferable due to high efficiency of the used x-ray detector. On the other hand, in the chosen electron energy range, for iridium only a partial ionization of the N-shell is possible. Here, the M-Nn DR process results with structures at photon energy of about 2.3 keV (iridium-M x-ray series) and it is below the range of high efficiency of the used detector. Therefore, the presented article is focused on the DR structures of cerium.

We have investigated the DR in cerium ions during two data collections. Firstly, we have used a buffer gas of neon with residual pressure at the level of 1.4×10^{-9} mbar. Secondly, we have closed the buffer gas inlet and measured the cerium DR spectrum at the base level of background pressure of 2.95×10^{-10} mbar.

2.2. Theoretical calculations

In order to theoretically describe the process discussed, an extended notation is used in the equation depicting the DR scheme:

$$e^- + |i\rangle \rightarrow |d\rangle \rightarrow |f\rangle + \hbar\omega. \tag{2}$$

Here, $|i\rangle$ denotes the initial state of the ion A^{q+}, $|d\rangle$ represents the intermediate excited state of the ion $A^{(q-1)+*}$, and $|f\rangle$ the final state of the ion $A^{(q-1)+}$ subsequent to the emission of a photon with an energy of $\hbar\omega$.

The DR resonant strengths (S_{DR}) were calculated based on the two-step model [27]:

$$S_{\mathrm{DR}}\left[\mathrm{cm^2 eV}\right] = \frac{2\pi^2\hbar^2}{p_e^2}\frac{g_d}{2g_i} \times \frac{\Gamma_a(|d\rangle \rightarrow |i\rangle)\Gamma_r(|d\rangle \rightarrow |f\rangle)}{\Gamma_a^{\mathrm{total}} + \Gamma_r^{\mathrm{total}}}, \tag{3}$$

where p_e is electron momentum, g_i, g_d are the statistical weights of $|i\rangle$ and $|d\rangle$, $\Gamma_a(|d\rangle \rightarrow |i\rangle)$ and $\Gamma_r(|d\rangle \rightarrow |f\rangle)$ are Auger and radiative width of a particular transition, respectively. $\Gamma_a^{\mathrm{total}} + \Gamma_r^{\mathrm{total}}$ contains the respective sum over all transitions in the calculated loop.

The (FAC, [28]) was used for calculations in UTA mode. This mode uses a relativistic configuration average approach known as spin orbit split array, explained in more detail in [29, 30], to calculate the electronic structure. By skipping the angular momentum couplings and grouping the full detailed fine structure into relativistic sub-configurations, the UTA mode significantly reduces the number of intermediate and final states by more than an order of magnitude. Although this results in a loss of detail, it enables the feasibility of complex calculations and allows for rough comparisons and structure identification. It is important to note that the UTA mode may yield modestly different branching ratios compared to full calculations, but the energy positions of the main structures remain predominantly accurate. It allows quick identification of the active charge state for particular resonance what makes it highly useful in this study. However, there is a low accuracy of the resonance strength calculation. Therefore, further within this article the results of cross section calculation for particular charge state and electron energy regime were scaled, without specifying the scaling parameters, to facilitate comparison with the experimental results. The UTA mode has been benchmarked by several groups comparing UTA-based opacity and emissivity spectra with full detail fine structure calculations [29, 31] for a wide range of elements and charge states. FAC also includes the sub-configuration averaged distorted wave method to apply the distorted wave approximation to the UTA-configuration-average wave functions, providing collisional ionization cross-sections [32, 33].

To provide a comprehensive analysis of the radiation structure arising from the L-Mn DR process in cerium ions, the following range of ion charge states from $q = 41+$ (Cl-like) to $q = 32+$ (Fe-like) were considered. The recombination was considered as an L-Mn transition, where n varied for each transition (M, N, O, P). The computational script included a simulation of the complete cascades following the final state, accounting for all possible Auger de-excitation channels. It

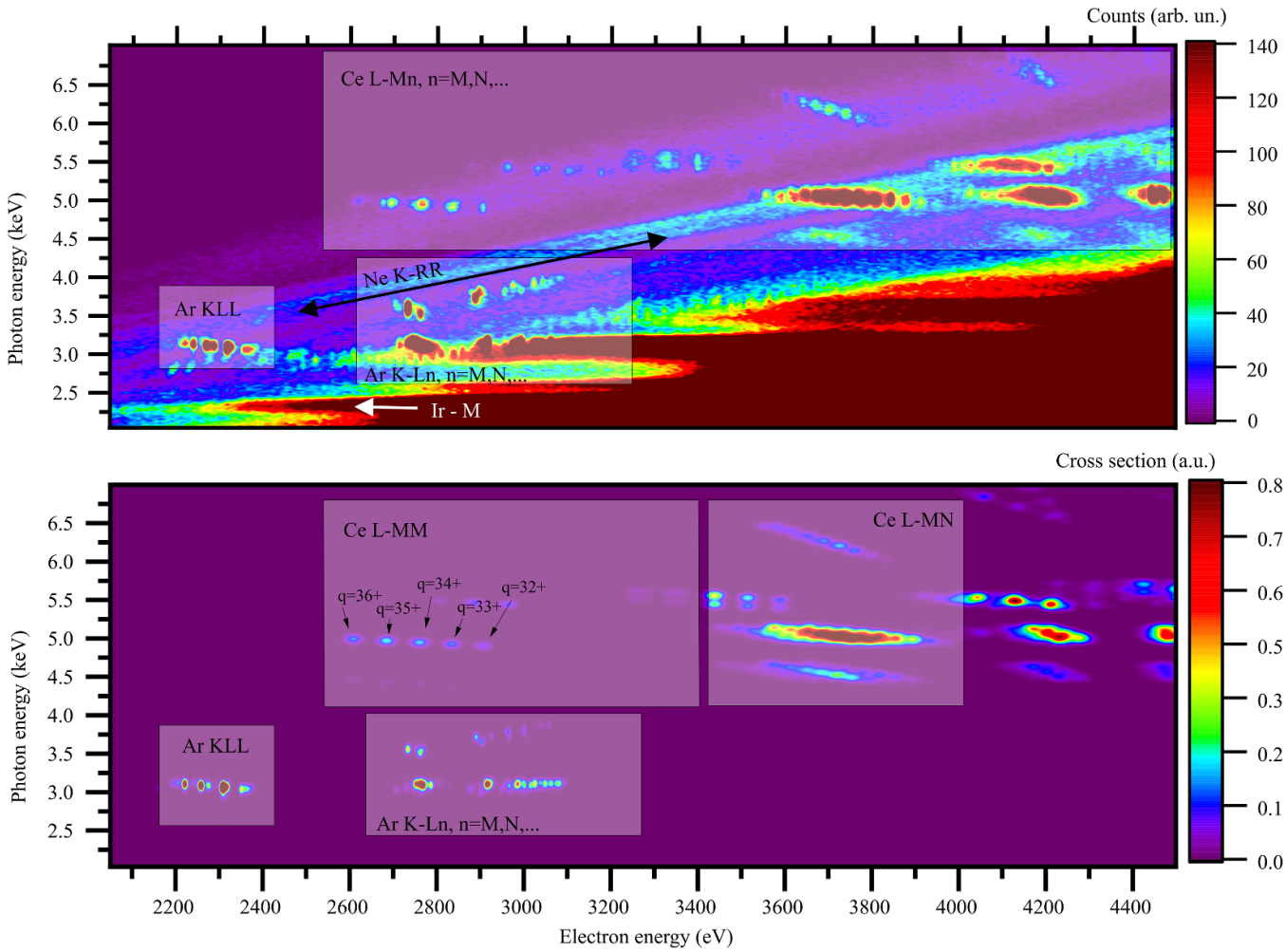

Figure 3. The comparison of experimental data and theoretical calculation. Top: The data collected for scanned electron energy in the range of 2000–4500 eV ($\Delta E_e = 10$ eV); the measurement time was approximately 28 hours, neon gas at the level of 1.4×10^{-9} mbar [25]. Bottom: results of FAC calculations done with the use of UTA; the intensity has been modified accordingly to simulate the changing charge state distribution in different electron energy regimes.

should be noted that Auger decay, subsequent to the DC step, is a highly competitive process alongside DR.

3. Results of DR structures of cerium

A goal of the presented experiment is to investigate the DR structure of cerium ions and demonstrate that DR calculations carried out in the UTA mode can effectively contribute to the identification of charge states in the experimental spectra. The measurement was performed by scanning the electron energy from 2000 eV to 4500 eV. A relatively long ionization time of 2000 ms was set to achieve a high degree of ionization for heavy cerium ions.

The measurement results for data collection with neon gas at the level of 1.4×10^{-9} mbar are presented in the top panel of figure 3. In this figure the DR resonances for argon ions are also observed. Argon, as a component of the atmospheric air (approximately 1%), is always present in trace amounts inside the trap. The DR structures for argon ions have already been deeply analyzed in our laboratory [24]. On the one hand, they served as a calibration benchmark for photon energy. On the other hand, it was used to calibrate the spectra on the low energy range (below 3000 eV) by comparing with previous [24] DR calculations made with FAC. To complement the calibration on medium to high energies, the radiative recombination to the K-shell of bare and H-like neon ions (Ne K-RR, indicated in figure 3) was fitted above 2800 eV of electron beam energy. Note that the free electron energy in RR is defined by $E_{e^-} = E_\gamma - E_b$, where E_{e^-}, E_γ and E_b are the electron energy, photon energy and binding energy, respectively. As the binding energy comes from a one-electron system, the theoretical value is sufficiently accurate for calibration purposes.

In the spectrum presented in figure 3 the presence of iridium ions is manifested by a line at approximately 2.3 keV. This corresponds to the iridium-M series radiation. Due to the fact that iridium is a heavy element ($Z = 77$), only a partial ionization

of the N-shell is possible for the electron energy chosen. On the other hand, the spectrum (figure 3) shows rich structures of the L-Mn DR resonances of cerium ($Z = 58$).

In the context of this article the most important part of the observed spectrum shown in figure 3 comprises the unique DR signatures of the cerium ions. It shows detailed patterns starting from around 2600 eV of electron energy and going up to the highest energies measured. The resulting photons from the DR processes range from 4 to 6.5 keV, depending on the deexcitation channels for DR processes in various ion charge states.

In the presented picture, each electron energy delivers an independent data set. During the scanning mode of the electron energy applied in this experiment, the EBIT trap was opened after each energy scan. Then, the voltage of the central electrode (and thus the electron energy E_e, as shown in figure 2) was incremented, and data were collected for the subsequent electron energy. As a result, the ion charge state distribution is expected to vary. At higher energies, the electron beam density is increased, leading to higher count rates for all ion-electron processes, including DR.

The top panel of figure 3 displays the experimental data, while the bottom panel shows the results obtained from FAC calculations. Here, again the DR structures of both argon and cerium ions are illustrated. At the bottom panel, for varying ranges of electron energy and photon energy, the charge state distribution of the involved argon or cerium ions was selected individually. This was done to present the most accurate display as to compare to the experimental data shown above it. Therefore, for argon K-LL structure the charge states from He-like to B-like were included. For argon K-Ln, $n = \mathrm{M}, \mathrm{N}, \ldots$ only two charge states were selected (Li-like and Be-like). In case of the cerium L-MM structure five charge states used in calculations are labeled at the graph (bottom panel of figure 3). For the higher resonant groups of cerium DR all charge states from $q = 32+$ up to $q = 41+$ were included with varying charge state distribution in order to reproduce experimental data.

4. Discussion

In order to compare the charge state distribution of the cerium ions at the two residual pressure levels of 1.4×10^{-9} mbar and 2.9×10^{-10} mbar, two distinct DR resonant groups were selected. These two groups are presented on the top panels of figures 4(a) and (b). These groups form a part of rich structures and can be also found at the top panel of figure 3. These selected x-ray spectra of the resonant structures collected for two vacuum levels were then projected on the electron energy axis. This way, the intensity of the observed DR structures across the two data collections was assessed (see bottom panels of figures 4(a) and (b)). Therefore, the bottom panels present a comparison of the intensity of the DR radiation for various charge states for two examined residual pressure levels. Results of calculations done in UTA, shown here as bars, served for identification of the active ion charge state.

The main DR peaks were fitted with standard Gaussian profiles. The fits were made with the experimental data corresponding to the residual pressure of 2.95×10^{-10} mbar. The experimental peak energies are listed in table 1 and compared to the UTA energies calculated with FAC. Only the mains peaks of the theoretical calculations were considered for the resonance identification, i.e. the peaks with an intensity above 30% of the main peak intensity. The double excited intermediate configuration is included in the last column of the table. Only resonances from the L-MM and L-MN structures were tabulated, as the emissions from the different charge states for the L-MO and L-MP structures are too blended to be identified individually. The listed experimental uncertainties are derived from a combination of one standard deviation from fit with the systematic of 4 eV from the electron energy calibration process involving theoretical calculations. For most of the resonances in the experimental data, there is a distinct correspondent resonance energy given by the theoretical calculations. These calculations do not take into account all of the possible angular momentum couplings, so the number of resulting resonances is clearly diminished. This approximation, however, is enough to obtain energies very close to the mean value of the correspondent complex DR structures. On the other hand, while the UTA-method predictions of DR do not provide the details of the array of resonances that forms each experimental peak, the UTA centroids are still in good agreement with experimental peaks positions. The benefit of this trade-off is time reduction. While FAC-UTA calculations of L-MN takes seconds to minutes, the time duration of the standard full-angular-coupling estimates to from hours to days, depending on the charge state. Comparing the experimental and theoretical energies, the FAC-UTA calculations are in agreement with all the experimental fitted values within less than 30 eV.

In figure 4, the cerium L-MM DR group is presented and analysed. A clear separation of the resonances originating from distinct charge states makes it ideal for investigation of differences in the charge state distribution. The red solid line, in the bottom panel of figure 4(a), is indicative of lower residual pressure and demonstrates a preference for higher charge states. In this case $q = 36+$ and $q = 35+$ states exhibit higher intensities under lower residual pressure conditions, whereas $q = 34+$, $q = 33+$ and $q = 32+$ states maintain at relatively comparable levels across both data collections.

In figure 4(b) the main cerium L-MN DR group is presented. It is important to mention that production of these DR resonances occurs at higher electron energies than the resonances presented in figure 4(a). With the increased electron energy, ionization becomes more efficient and higher ionization thresholds are achieved. Therefore, the active charge states in figure 4(b) tend to be more ionized in comparison to figure 4(a).

Data presented in figure 4(b) clearly presents that the intensity of the L-MN resonant structure collected for lower residual pressure causes the reduction of the intensity of resonances for lower charge states, particularly for $q = 35+$, $q = 34+$ and $q = 33+$. Therefore, a tendency to enhance

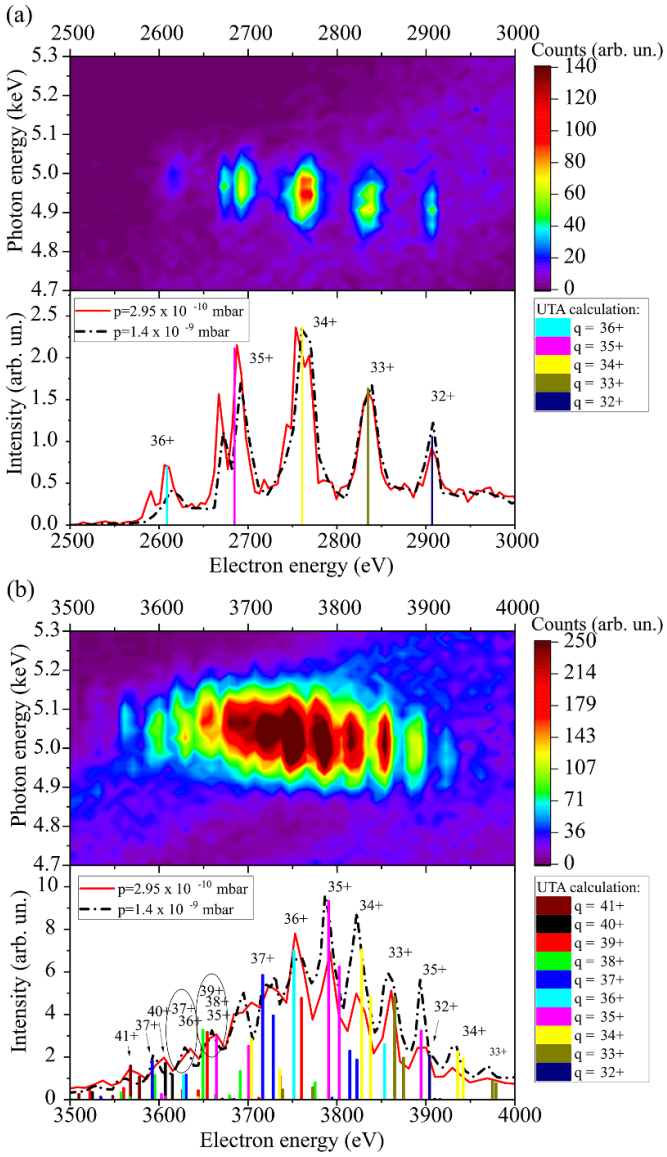

Figure 4. Top panels: selected parts of the experimental data presented in figure 3. Bottom panels: projections of the x-ray spectra on the electron energy axis for two residual pressure levels (2.95×10^{-10} mbar—red solid line, 1.4×10^{-9} mbar—black dashed line). Bars shown in bottom panels present results of the UTA calculations for various cerium charge states. (a) represents the cerium L-MM resonant group, (b) represents the cerium L-MN resonant group.

the lower charge states for a higher residual pressure (black dashed line) is demonstrated in the bottom panel of figure 4(b). The resonances for higher charge states, which are visible at lower electron energies, can be observed at similar intensity level for both vacuum conditions. However, one has to pay a special attention to peaks around 3570 eV and 3600 eV. Position of these peaks depends on the residual pressure in EBIT. It can be explained by the increase of the $q = 41+$ and $q = 40+$ population, if the vacuum conditions are better. In case of worse vacuum $q = 41+$ and $q = 40+$ seem to be not active and ion charge states responsible for the production of peaks around 3570 eV and 3600 eV are $q = 39+$ and $q = 37+$. Hence, again like for figure 4(a), data collected under the lower residual pressure condition demonstrates a preference for higher charge states.

Table 1. Experimental energies of the Ce DR resonances fitted with a standard gausian profile. The FAC-UTA calculations used to make the resonance identification are also presented, with the respective charge state, theoretical energy and intermediate configuration. For the intermediate configuration, the 1*s* orbital is full and is omitted. The fits were made with the experimental data corresponding to the residual pressure of 2.95×10^{-10} mbar.

Process	Charge state	E_{exp}	$E_{\text{FAC-UTA}}$	Intermediate configuration
L-MM	36+	2590 ± 5	2609.5	$2s^2_{1/2}\,2p^2_{1/2}\,2p^3_{3/2}\,3s^2_{1/2}3p^2_{1/2}\,3p^4_{3/2}\,3d^2_{5/2}$
		2610 ± 4		
	35+	2668 ± 4	2685.4	$2s^2_{1/2}\,2p^2_{1/2}\,2p^3_{3/2}\,3s^2_{1/2}3p^2_{1/2}\,3p^4_{3/2}\,3d^3_{5/2}$
		2689 ± 4		
	34+	2760 ± 4	2760.2	$2s^2_{1/2}\,2p^2_{1/2}\,2p^3_{3/2}\,3s^2_{1/2}3p^2_{1/2}\,3p^4_{3/2}\,3d^4_{5/2}$
	33+	2836 ± 4	2834.1	$2s^2_{1/2}\,2p^2_{1/2}\,2p^3_{3/2}\,3s^2_{1/2}3p^2_{1/2}\,3p^4_{3/2}\,3d^5_{5/2}$
	32+	2907 ± 4	2906.9	$2s^2_{1/2}\,2p^2_{1/2}\,2p^3_{3/2}\,3s^2_{1/2}3p^2_{1/2}\,3p^4_{3/2}\,3d^6_{5/2}$
L-MN	41+	3562 ± 6	3540.4	$2s^2_{1/2}\,2p^2_{1/2}\,2p^3_{3/2}\,3s^2_{1/2}3p^2_{1/2}\,3p^3_{3/2}\,3d^1_{3/2}\,4d^1_{3/2}$
	41+		3552.3	$2s^2_{1/2}\,2p^2_{1/2}\,2p^3_{3/2}\,3s^2_{1/2}3p^2_{1/2}\,3p^3_{3/2}\,3d^1_{3/2}\,4d^1_{5/2}$
	40+	3596 ± 4	3611.1	$2s^2_{1/2}\,2p^2_{1/2}\,2p^3_{3/2}\,3s^2_{1/2}3p^2_{1/2}\,3p^4_{3/2}\,3d^1_{5/2}\,4d^1_{3/2}$
	37+		3593.2	$2s^2_{1/2}\,2p^2_{1/2}\,2p^3_{3/2}\,3s^2_{1/2}3p^2_{1/2}\,3p^4_{3/2}\,3d^3_{3/2}\,3d^1_{5/2}\,4p^1_{1/2}$
	37+	3628 ± 4	3630.7	$2s^2_{1/2}\,2p^2_{1/2}\,2p^3_{3/2}\,3s^2_{1/2}3p^2_{1/2}\,3p^4_{3/2}\,3d^3_{3/2}\,3d^1_{5/2}\,4p^1_{3/2}$
	36+		3627.1	$2s^2_{1/2}\,2p^2_{1/2}\,2p^3_{3/2}\,3s^2_{1/2}3p^2_{1/2}\,3p^4_{3/2}\,3d^4_{3/2}\,3d^1_{5/2}\,4p^1_{1/2}$
	39+	3660 ± 4	3646.7	$2s^2_{1/2}\,2p^2_{1/2}\,2p^3_{3/2}\,3s^2_{1/2}3p^2_{1/2}\,3p^4_{3/2}\,3d^1_{3/2}\,3d^1_{5/2}\,4d^1_{3/2}$
	38+		3664.9	$2s^2_{1/2}\,2p^2_{1/2}\,2p^3_{3/2}\,3s^2_{1/2}3p^2_{1/2}\,3p^4_{3/2}\,3d^3_{3/2}\,4d^1_{5/2}$
	35+		3663.7	$2s^2_{1/2}\,2p^2_{1/2}\,2p^3_{3/2}\,3s^2_{1/2}3p^2_{1/2}\,3p^4_{3/2}\,3d^4_{3/2}\,3d^2_{5/2}\,4p^1_{3/2}$
		3692 ± 4		
	37+	3722 ± 4	3716.5	$2s^2_{1/2}\,2p^2_{1/2}\,2p^3_{3/2}\,3s^2_{1/2}3p^2_{1/2}\,3p^3_{3/2}\,3d^3_{3/2}\,3d^1_{5/2}\,4d^1_{3/2}$
	37+		3728.6	$2s^2_{1/2}\,2p^2_{1/2}\,2p^3_{3/2}\,3s^2_{1/2}3p^2_{1/2}\,3p^3_{3/2}\,3d^3_{3/2}\,3d^1_{5/2}\,4d^1_{5/2}$
	36+	3757 ± 4	3750.7	$2s^2_{1/2}\,2p^2_{1/2}\,2p^3_{3/2}\,3s^2_{1/2}3p^2_{1/2}\,3p^3_{3/2}\,3d^4_{3/2}\,3d^1_{5/2}\,4d^1_{3/2}$
	35+	3790 ± 4	3788.4	$2s^2_{1/2}\,2p^2_{1/2}\,2p^3_{3/2}\,3s^2_{1/2}3p^2_{1/2}\,3p^3_{3/2}\,3d^4_{3/2}\,3d^2_{5/2}\,4d^1_{3/2}$
	35+		3800.1	$2s^2_{1/2}\,2p^2_{1/2}\,2p^3_{3/2}\,3s^2_{1/2}3p^2_{1/2}\,3p^3_{3/2}\,3d^4_{3/2}\,3d^2_{5/2}\,4d^1_{5/2}$
	34+	3822 ± 4	3825.5	$2s^2_{1/2}\,2p^2_{1/2}\,2p^3_{3/2}\,3s^2_{1/2}3p^2_{1/2}\,3p^3_{3/2}\,3d^4_{3/2}\,3d^3_{5/2}\,4d^1_{3/2}$
	34+		3835.8	$2s^2_{1/2}\,2p^2_{1/2}\,2p^3_{3/2}\,3s^2_{1/2}3p^2_{1/2}\,3p^3_{3/2}\,3d^4_{3/2}\,3d^3_{5/2}\,4d^1_{5/2}$
	33+	3860 ± 4	3861.9	$2s^2_{1/2}\,2p^2_{1/2}\,2p^3_{3/2}\,3s^2_{1/2}3p^2_{1/2}\,3p^3_{3/2}\,3d^4_{3/2}\,3d^4_{5/2}\,4d^1_{3/2}$
	35+	3894 ± 4	3893	$2s^2_{1/2}\,2p^2_{1/2}\,2p^3_{3/2}\,3s^2_{1/2}3p^2_{1/2}\,3p^3_{3/2}\,3d^4_{3/2}\,3d^2_{5/2}\,4f^1_{5/2}$
	32+		3905.4	$2s^2_{1/2}\,2p^2_{1/2}\,2p^3_{3/2}\,3s^2_{1/2}3p^2_{1/2}\,3p^3_{3/2}\,3d^4_{3/2}\,3d^5_{5/2}\,4d^1_{5/2}$
	34+	3929 ± 5	3932.9	$2s^2_{1/2}\,2p^2_{1/2}\,2p^3_{3/2}\,3s^2_{1/2}3p^2_{1/2}\,3p^3_{3/2}\,3d^4_{3/2}\,3d^3_{5/2}\,4f^1_{5/2}$
	34+		3938.2	$2s^2_{1/2}\,2p^2_{1/2}\,2p^3_{3/2}\,3s^2_{1/2}3p^2_{1/2}\,3p^3_{3/2}\,3d^4_{3/2}\,3d^3_{5/2}\,4f^1_{7/2}$
	33+	3968 ± 5	3971.8	$2s^2_{1/2}\,2p^2_{1/2}\,2p^3_{3/2}\,3s^2_{1/2}3p^2_{1/2}\,3p^3_{3/2}\,3d^4_{3/2}\,3d^4_{5/2}\,4f^1_{5/2}$
	33+		3975.6	$2s^2_{1/2}\,2p^2_{1/2}\,2p^3_{3/2}\,3s^2_{1/2}3p^2_{1/2}\,3p^3_{3/2}\,3d^4_{3/2}\,3d^4_{5/2}\,4f^1_{7/2}$

5. Summary

The DR resonances exhibit a very rich structures which depend on the charge state distribution of active element. This distribution can be partly controlled by the gas pressure level inside the trap. It was vividly demonstrated in figures 3 and 4. We have observed and cataloged the main DR L-M*n* resonances of cerium charge states from 32+ to 40+ and provided their experimental energies values. These values were successfully compared with the calculated UTA energies. This way, it was also shown that DR calculations performed in UTA mode provides quick and reliable predictions for charge states identification. Although the UTA method is a rudimentary theoretical approximation, it can give valuable insights to the experimental data in spite of the complexity of the atomic processes.

Data availability statement

The data cannot be made publicly available upon publication because they are not available in a format that is sufficiently accessible or reusable by other researchers. The data that support the findings of this study are available upon reasonable request from the authors.

Acknowledgments

P A and F G acknowledge the FCT through Project Number UID/04559/2020 (LIBPhys), and contract No. UI/BD/151000/2021. This research has been carried out under the High Performance Computing Chair—a R&D

infrastructure (based at the University of Évora; PI: M Avillez), endorsed by Hewlett Packard Enterprise (HPE), and involving a consortium of higher education institutions (University of Algarve, University of Évora, New University of Lisbon, and University of Porto), research centres (CIAC, CIDEHUS, CHRC), enterprises (HPE, ANIET, ASSIMAGRA, Cluster Portugal Mineral Resources, DECSIS, FastCompChem, GeoSense, GEOtek, Health Tech, Starkdata), and public/private organizations (Alentejo Tourism-ERT, KIPT Colab). W B -N acknowledges the GET_INvolved Programme at FAIR/GSI (www.fair-center.eu/get_involved) and the JIPhD program through contract POWR.03.05.00-00-Z309/17-00.

ORCID iDs

W Biela-Nowaczyk https://orcid.org/0000-0002-8257-7801
F Grilo https://orcid.org/0000-0001-5777-1891
P Amaro https://orcid.org/0000-0002-5257-6728

References

[1] Hargreaves J, Moore S, Yuan G, Liu D, Tipping H, Abbott R, Tufnail J, Dawson H and Martin T L 2023 Microstructural modelling and characterisation of laser-keyhole welded eurofer 97 *Mater. Des.* **226** 111614
[2] Sales-Silva J V 2020 Exploring the s-process history in the galactic disk: cerium abundances and gradients in open clusters from the occam/apogee sample *Astrophys. J.* **926** 154
[3] Yang Y-H et al 2023 A lanthanide-rich kilonova in the aftermath of a long gamma-ray burst
[4] Tanvir N R *et al* 2017 The emergence of a lanthanide-rich kilonova following the merger of two neutron stars *Astrophys. J. Lett.* **848** L27
[5] Tanaka M *et al* 2023 Cerium features in kilonova near-infrared spectra: implication from a chemically peculiar star *Astrophys. J.* **953** 17
[6] Domoto N, Tanaka M, Kato D, Kawaguchi K, Hotokezaka K and Wanajo S 2022 Lanthanide features in near-infrared spectra of kilonovae
[7] Paulo Santos J P, Conceição Martins M C, Maria Costa A M, Pires Marques J P, Indelicato P and Parente F 2014 Theoretical determination of k x-ray transition energy and probability values for highly charged ions of lanthanum and cerium *Eur. Phys. J.* D **68** 244
[8] Ovsyannikov V P, Nefiodov A V, Yu Boytsov A, Yu Ramzdorf A, Stegailov V I, Tyutyunnikov S I and Levin A A 2021 Main magnetic focus ion source: device with high electron current density *Nucl. Instrum. Methods Phys. Res.*B **502** 23–28
[9] Ovsyannikov V P, Zschornack G, Großmann F, Heller R, Kentsch U, Kreller M, Landgraf S, Schmidt M and Ullmann F 2007 First investigations on the dresden EBIS-A *J. Phys.: Conf. Series* **58** 399–402
[10] Biedermann C, Radtke R, Seidel R and Pütterich T 2009 Spectroscopy of highly charged tungsten ions relevant to fusion plasmas *Phys. Scr.* **T134** 014026
[11] Neill P, Harris C, Safronova A S, Hamasha S, Hansen S, Safronova U I and Beiersdorfer P 2004 The study of x-ray m-shell spectra of w ions from the lawrence livermore national laboratory electron beam ion trap *Can. J. Phys.* **82** 931–42
[12] Morita S *et al* 2013 A study of tungsten spectra using large helical device and compact electron beam ion trap in NIFS **1545** 143–52
[13] Wong K L, May M J, Beiersdorfer P, Fournier K B, Wilson B, Brown G V, Springer P, Springer P A, Neill P A and Harris C L 2003 Determination of the charge state distribution of a highly ionized coronal au plasma *Phys. Rev. Lett.* **90** 235001
[14] Shah C *et al* 2021 High-resolution laboratory measurements of k-shell x-ray line polarization and excitation cross sections in helium-like s XV ions *Astrophys. J.* **914** 34
[15] Xiong G, Zhang J, Hu Z, Nakamura N, Li Y, Han X, Yang J and Zhang B 2013 Kll dielectronic-recombination measurement for Li-like to O-like gold *Phys. Rev.* A **88** 042704
[16] Schneider M B, Knapp D A, Chen M H, Scofield J H, Beiersdorfer P, Bennett C L, Henderson J R, Levine M A and Marrs R E 1992 Measurement of the lmm dielectronic recombination resonances of neonlike gold *Phys. Rev.* A **45** R1291–4
[17] Yao K, Geng Z, Xiao J, Yang Y, Chen C, Fu Y, Lu D, Hutton R and Zou Y 2010 Kll dielectronic recombination resonant strengths of He-like up to O-like xenon ions *Phys. Rev.* A **81** 022714
[18] Hu Z, Li Y and Nakamura N 2013 Resonance strength for kll dielectronic recombination of hydrogenlike krypton *Phys. Rev.* A **87** 052706
[19] Lindroth E, Orban I, Trotsenko S and Schuch R 2020 Electron-impact recombination and excitation rates for charge-state-selected highly charged si ions *Phys. Rev.* A **101** 062706
[20] Liyi G 2020 x-ray spectra of the Fe-L complex *Astron. Astrophys.* **641** 9
[21] Shah C, López-Urrutia J R C, Gu M F, Pfeifer T, Marques J, Grilo F, Paulo Santos J P and Amaro P 2019 Revisiting the fe XVII line emission problem: Laboratory measurements of the 3s–2p and 3d–2p line-formation channels *Astrophys. J.* **881** 100
[22] Grilo F, Shah C, Kühn S, Steinbrügge R, Fujii K, Marques J, Feng Gu M, Paulo Santos J, Crespo López-Urrutia J R and Amaro P 2021 Comprehensive laboratory measurements resolving the lmm dielectronic recombination satellite lines in ne-like fe XVII ions *Astrophys. J.* **913** 6
[23] Biela-Nowaczyk W, Amaro P, Grilo F, La Mantia D, Tanis J and Warczak A 2023 Hypersatellite K_α production in trapped ar ions at KK trielectronic recombination energies *Atoms* **11** 3
[24] Biela-Nowaczyk W, Amaro P, Grilo F and Warczak A 2022 Higher-order recombination processes in argon ions observed via x-ray emission in an ebit *Atoms* **11** 12
[25] Biela-Nowaczyk W 2022 Rzadkie procesy atomowe w cięż Kich Jonach Badane przy Pomocy aparatury Ebit *PhD Dissertation* Faculty of Physics Astronomy and Applied Computer Science of the Jagiellonian Uiversity
[26] DREEBIT Team 2012 Instruction manual ion irradiation facility s (Version 1.1)
[27] Chintan S 2015 Measuring and modeling of anisotropic and polarized x-ray emission following resonant recombination into highly charged ions *PhD Dissertation* combined faculties of the natural sciences and mathematics of the ruperto-carola-university of heidelberg
[28] Gu M F 2008 The flexible atomic code *Can. J. Phys.* **86** 675–89

[29] Poirier M 2018 Opacity calculations in X and XUV range using a detailed atomic code *Contrib. Plasma Phys.* **58** 1005–14

[30] Bauche J, Bauche-Arnoult C and Klapisch M 1988 Transition arrays in the spectra of ionized atoms (*Advances in Atomic and Molecular Physics* vol 23) ed D Bates and B Bederson (Academic) pp 131–95

[31] Hansen S B 2011 Configuration interaction in statistically complete hybrid-structure atomic models *Can. J. Phys.* **89** 633–8

[32] Jonauskas V, Kynienė A, Merkelis G, Gaigalas G, Kisielius R, Kučas S, Masys L P, Radžiūtė L and Rynkun P 2015 Contribution of high-shells to electron-impact ionization processes *Phys. Rev.* A **91** 012715

[33] Jin F, Borovik A, Ebinger B and Schippers S 2020 Hybrid subconfiguration-average and level-to-level distorted-wave treatment of electron-impact single ionisation of w_{15+} and w_{16+} *J. Phys. B: At. Mol. Opt. Phys.* **53** 175201